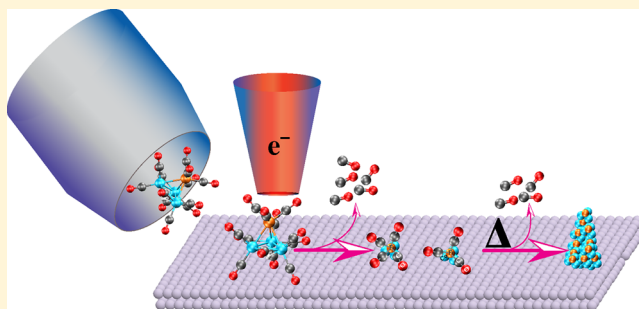


Electron Induced Surface Reactions of $\text{HFeCo}_3(\text{CO})_{12}$, a Bimetallic Precursor for Focused Electron Beam Induced Deposition (FEBID)

Ragesh Kumar T P,[†] Ilyas Unlu,[‡] Sven Barth,[§] Oddur Ingolfsson,[†] and D. Howard Fairbrother^{*,‡,§}[†]Science Institute and Department of Chemistry, University of Iceland, Dunhagi 3, 107 Reykjavik, Iceland[‡]Department of Chemistry, Johns Hopkins University, Baltimore, Maryland 21218, United States[§]Inst. of Materials Chemistry, TU Wien, Getreidemarkt 9/BC/02, A-1060 Wien, Austria

Supporting Information

ABSTRACT: The use of bimetallic precursors in focused electron beam induced deposition (FEBID) allows mixed metal nanostructures with well-defined metal ratios to be generated in a single step process. $\text{HFeCo}_3(\text{CO})_{12}$ is an example of one such bimetallic precursor that has previously been shown to form deposits with unusually high metal content (>80%) as compared to that of typical FEBID deposits (<30% metal content). To better understand the elementary bond breaking steps involved in FEBID of $\text{HFeCo}_3(\text{CO})_{12}$, we have employed a UHV surface science approach to study the effect of electron irradiation on nanometer thick films of $\text{HFeCo}_3(\text{CO})_{12}$ molecules. Using a combination of in situ X-ray photoelectron spectroscopy and mass spectrometry, we observed that the initial step of electron induced $\text{HFeCo}_3(\text{CO})_{12}$ dissociation is accompanied by desorption of $\sim 75\%$ of the CO ligands from the precursor. A comparison with recent gas phase studies of $\text{HFeCo}_3(\text{CO})_{12}$ indicates that this process is consistent with a dissociative ionization process, mediated by the secondary electrons produced by interaction of the primary beam with the substrate. The loss of CO ligands from $\text{HFeCo}_3(\text{CO})_{12}$ in the initial dissociation step creates partially decarbonylated intermediates, $\text{HFeCo}_3(\text{CO})_x$ ($x_{\text{avg.}} \approx 3$). During a typical FEBID process, further electron exposure or thermal reactions can further transform these intermediates. In our UHV surface science approach, the effect of these two processes can be studied in isolation and identified. Under the influence of further electron irradiation, XPS data reveals that the remaining CO ligands in the partially decarbonylated intermediates decompose to form residual carbon and iron oxides, suggesting that those CO ligands that desorbed in the initial step are lost predominantly from the Co atoms. However, annealing experiments demonstrate that CO ligands in the partially decarbonylated intermediates desorb under vacuum conditions at room temperature, leaving behind films that are free of almost any carbon or oxygen contaminants. This combination of efficient CO desorption during the initial dissociation step, followed by thermal CO desorption from the partially decarbonylated $\text{HFeCo}_3(\text{CO})_x$ ($x_{\text{avg.}} \approx 3$) intermediates provide a rationale for the high metal contents observed in FEBID nanostructures created from $\text{HFeCo}_3(\text{CO})_{12}$.



INTRODUCTION

Focused electron beam induced deposition (FEBID)^{1,2} is a predominantly vacuum-based, direct-write, three-dimensional nanofabrication technique based on electron induced dissociation of volatile precursor molecules. In FEBID, a high-energy electron beam is focused onto a substrate and dissociates precursor molecules, transiently adsorbed on the substrate surface, into volatile and nonvolatile fragments. The volatile fragments can be pumped away, while the nonvolatile fragments becoming incorporated into a growing deposit. For metal deposits, volatile organometallics are the most commonly used precursors. Compared to other vacuum-based nanofabrication techniques like electron beam lithography (EBL) and extreme ultraviolet and ultraviolet lithography (EUVL and UVL, respectively),^{3,4} FEBID has several useful advantages. For example, it can directly write an almost unlimited array of free-standing 3-D nanostructures on any substrate, irrespective of its

geometry. Moreover, FEBID does not need any resist layer or solvent for deposition¹ and has been successfully used in a number of technological and scientific applications, where conventional lithography is not suitable. For example, using the popular Pt precursor MeCpPtMe_3 , FEBID has been used to repair photolithography masks,^{5–7} while $\text{W}(\text{CO})_6$, $\text{Co}_2(\text{CO})_8$, and MeCpPtMe_3 precursors have been used to produce custom tips for scanning tunneling^{8,9} and atomic force microscopes,^{10,11} and FEBID of $\text{Me}_2\text{Au}(\text{acac})$, $\text{W}(\text{CO})_6$ and tetraethyl-ortho-silicate $\text{Si}(\text{OC}_2\text{H}_5)_4$ precursors has provided a route to fabricate and modify nanophotonic and nanoplasmonic devices.^{12–14}

Received: August 29, 2017

Revised: November 29, 2017

Published: December 14, 2017

In the FEBID applications mentioned above, nanostructures are fabricated using homometallic precursors. Typical homonuclear organometallic precursors used in FEBID include MeCpPtMe_3 , $\text{Au}(\text{acac})\text{Me}_2$, $\text{Pt}(\text{PF}_3)_4$, $\text{W}(\text{CO})_6$, and $\text{Co}(\text{CO})_3\text{NO}$.¹ However, for some nano-technology applications such as magnetic data storage, nanoelectronics, and information technology it is desirable to fabricate bimetallic alloy nanostructures. The fabrication of bimetallic nanostructures using FEBID is a relatively recent development,¹⁵ which has been accomplished principally by codepositing different metals simultaneously from separate homonuclear precursors using dual or multichannel precursor gas injection systems.^{16–18} However, in this approach, it is difficult to exert good control over the composition of the deposit, and the reproducibility is generally poor.¹⁸ To overcome these limitations, Porrati et al.¹⁹ have, for the first time, used a bimetallic precursor: $\text{HfFeCo}_3(\text{CO})_{12}$. This volatile organometallic precursor was first synthesized by Chini et al.²⁰ and has been used in chemical vapor deposition (CVD)²¹ and photochemical vapor deposition (PCVD)²² to fabricate FeCo thin films. $\text{HfFeCo}_3(\text{CO})_{12}$ has also been used to prepare magnetic ferrofluids, which have applications in magnetically controlled drug delivery²³ as well as building nanoscale devices like nanomotors, nanogenerators, and nanopumps.²⁴ In FEBID, $\text{HfFeCo}_3(\text{CO})_{12}$ was used to fabricate FeCo magnetic alloy nanostructures with a well-defined metal ratio, matching the stoichiometry of the precursor.¹⁹ Hall magnetometric measurements on 50×250 nm FeCo nanobars demonstrated that the fabricated FeCo structure was ferromagnetic,¹⁹ an important property for building magnetic data storage devices. A potential application for these data storage devices could be as building blocks in the creation of nanosized read/write heads for magnetic recordings.²⁵ The current read/write speed of hard disk drive heads is ~ 200 Gbit/in², and by decreasing the read/write head size to under 20 nm, the read/write speed could increase to 1000 Gbit/in².²⁵ Moreover; fundamental investigations on 3-D geometries that are not accessible by current crystallization or other template-based techniques can be facilitated by FEBID, opening up the possibility to study the physics of 3-D nanomagnets as well as their potential applications.²⁶

Although FEBID has many attractive features as a direct-write strategy for nanofabrication, it has not yet attained its full potential, in large part due to issues such as lateral broadening of deposited structures²⁷ and the presence of unacceptable levels of organic impurities in the deposits.^{1,28} With respect to the issue of contamination, several important properties of FEBID deposits such as conductivity,^{29–31} magnetic behavior,³² and catalytic activity²⁹ are adversely affected by the unwanted codeposition of organic impurities (commonly carbon and oxygen) in the FEBID deposits. The major cause of impurities in the FEBID deposits arises from incomplete removal of ligands during the electron stimulated deposition of the precursor molecules, although secondary reactions involving residual water and/or hydrocarbons in the deposition chamber also contribute. To date, almost all FEBID precursors were initially designed for CVD, which works on the basis of thermal as opposed to electron induced dissociation.³³ This in turn leaves significant potential for performance improvement in targeted precursors designed specifically for electron induced decomposition in FEBID.

An important step in the design of new precursors specifically tailored for FEBID is to develop a more fundamental understanding of how their electron induced

decomposition proceeds. Studies to date indicate that precursor dissociation is mediated mainly by low energy secondary electrons generated by the interaction of the primary electrons with the substrate/deposit, rather than through direct interaction of precursor molecules with the primary beam.^{34–36} These low energy electrons ($< \approx 100$ eV) can cause decomposition of adsorbed precursor molecules through four distinct processes; dissociative electron attachment (DEA), dissociative ionization (DI), and neutral or dipolar dissociation upon electron excitation (ND and DD, respectively).^{36–42} In DEA, a free electron is resonantly captured by the respective molecule to form a transient negative ion (TNI), which then relaxes, either by re-emission of the electron (autodetachment) or by dissociation forming a negative ion and one or more neutral species. DEA is most efficient at very low energies, i.e., around 0 eV.³⁶ DI, on the other hand, is a nonresonant process with an onset at or above the ionization energy of the molecule and generally reaches a maximum efficiency somewhere between 50 and 100 eV.³⁶ In DI, the fragments are a positive ion and one or more neutrals. ND is also a nonresonant process that sets in at the threshold of the first molecular electronic excitation, producing two or more neutral, mainly radical fragments.³⁶ However, due to the difficulty in detecting neutral fragments, no direct experimental data on ND of FEBID precursors is currently available. Finally, DD is generally an inefficient dissociation process initiated by electron excitation(s) within the parent molecules and results in a positive and a negative fragment being formed.³⁶

The susceptibility of FEBID precursors to these processes can be best studied in the gas phase under single collision conditions, where charged fragments generated from the interaction of electrons with precursor molecules can be identified, and their yields can be determined as a function of the incident electron energy. Importantly, such gas phase studies can differentiate between the individual low energy induced processes and may offer a basis to evaluate their relative efficiency and their branching ratios.³⁶ Recent gas phase studies on $\text{HfFeCo}_3(\text{CO})_{12}$ ^{43,44} have revealed an exceptional behavior of this compound with regards to DEA, showing a wide range of fragments and attachment cross sections up to energies 11 eV above its ionization energy, where the loss of all 12 CO ligands was observed. However, despite the extensive fragmentation observed in DEA, DI is the more efficient process with regards to the average number of CO molecules lost per incident electron interaction during $\text{HfFeCo}_3(\text{CO})_{12}$ fragmentation; in DEA it is 2–3, while in DI it ranges from 4 to 9.⁴⁵

In the current contribution, we employ a surface science approach under ultrahigh-vacuum (UHV) conditions to study electron induced surface reactions in nanometer thin films of $\text{HfFeCo}_3(\text{CO})_{12}$ precursor molecules. The principle techniques used for this study are X-ray photoelectron spectroscopy (XPS) and mass spectrometry (MS), used to monitor changes in the composition and bonding within the film as well as identify neutral gas phase species generated when thin films of $\text{HfFeCo}_3(\text{CO})_{12}$ are exposed to electrons with incident energies of 500 eV. Compared to gas phase studies, this approach offers offer a platform to study the deposition and decomposition of this precursor under condensed phase conditions that are closer to those in FEBID. Moreover, the UHV surface science experiments are conducted under cryogenic temperatures (-60 °C), where the evolution of a predeposited precursor film can be followed as the electron dose is increased, while in FEBID,

experiments are conducted at room temperature under steady-state conditions with a continuous precursor supply. As a result, the UHV surface science approach is better suited to identifying the sequence of elementary reaction steps experienced by precursor molecules during FEBID, including the identification of volatile fragments produced during the deposition process and the concomitant changes to the composition and bonding within the adsorbed precursor molecules. Compared to gas phase studies, surface science studies do not allow differentiation between individual processes such as DEA, DI, and DD, because precursor molecules are simultaneously exposed to secondary electrons with a range of energies. In conjunction with data from gas phase studies, however, these surface science studies have the potential to identify the initial electron induced mechanism of precursor dissociation in FEBID based on the initial step observed in the surface science studies as compared to the different fragments and their relative intensities observed in the gas phase.³⁶

Previously, we have used this UHV surface science approach to study electron induced reactions (and thermal reactions of intermediate species) of a wide variety of homonuclear organometallic complexes including MeCpPtMe₃,⁴⁶ Au(acac)Me₂,⁴⁷ Pt(PF₃)₄,⁴⁸ W(CO)₆,⁴⁹ Co(CO)₃NO,⁵⁰ (η^3 -C₃H₅)Ru(CO)₃Br,⁵¹ and cis-Pt(CO)₂Cl₂.⁵² In general, we have found that electron induced dissociation of precursor molecules proceeds in two steps. In the first step, electron stimulated decomposition of the precursor molecule leads to desorption of some ligands from the adsorbed precursor molecule, leaving behind a metal-containing intermediate bound to the substrate. If this intermediate is subject to further electron irradiation, remaining ligands typically undergo decomposition rather than desorption, and we believe that this process is the primary cause of organic impurities in FEBID deposits. In some instances, however, these intermediates are susceptible to thermal reactions, which generally lead to further ligand desorption and a concomitant improvement in the metal content. It should be noted that these studies are conducted at low substrate temperatures (typically <−120 °C) and on inert substrates (typically Au and a:C) so that any substrate effects are eliminated/minimized. In support of this assertion, we have routinely observed the same electron stimulated processes to occur, independent of the substrate.

The present study of HFeCo₃(CO)₁₂ was motivated in part by its use as the first bimetallic FEBID precursor and its exceptional behavior with regards to DEA,^{19,43} but also because it offers the ability to follow the fate of two dissimilar metal atoms simultaneously (using XPS) during the elementary reaction steps that underpin FEBID. FEBID deposits created from HFeCo₃(CO)₁₂ have also been shown to exhibit metal contents >80%, much higher than typically observed for homonuclear FEBID precursors.¹ In contrast, FEBID nanostructures created from a similar bimetallic precursor, H₂FeRu₃(CO)₁₃, in common with most FEBID precursors, exhibit significantly lower metal contents (<30%).⁴⁵ Consequently, fundamental studies on the elementary reactions of HFeCo₃(CO)₁₂ in FEBID may help to shed light on the structural aspects of organometallic precursors that promote efficient and complete ligand desorption and the creation of deposits with higher metal contents.

■ EXPERIMENTAL SECTION

Precursor Molecule. The synthesis of HFeCo₃(CO)₁₂ was carried out using a procedure slightly modified from the one

described by Chini et al.²⁰ All handling and synthesis procedures were carried out under an inert atmosphere using Schlenk and glovebox techniques to prevent oxidation. Co₂(CO)₈, Fe(CO)₅, HCl, DCl, D₂O, and acetone were purchased from Sigma-Aldrich. Solvents were degassed before use.

In a typical synthesis procedure, 0.50 g (2.6 mmol) of Fe(CO)₅ and 1.51 g (4.4 mmol) Co₂(CO)₈ were combined in a three-neck flask and 4.8 mL of acetone was added dropwise. After stirring this dark solution at 40 °C for 2 h, the temperature was increased to 60 °C for 12 h. All volatile components were removed under reduced pressure (2×10^{-2} mbar; 25 °C) and collected in a cooling trap (liquid N₂). The dark solid residue was dissolved in 10 mL of degassed water and filtered in 15 mL of HCl conc. (37%), although the yield could be increased by using 5 mL of degassed water to transfer most of the complex to the hydrochloric acid. The mixture of the precipitated raw product and HCl was stirred for 1 h at room temperature before the dark purple raw product was separated from the acidic solution via filtration and dried overnight under reduced pressure. Dark purple needles of HFeCo₃(CO)₁₂ were obtained after recrystallization from toluene. The products were then kept under dynamic vacuum ($\sim 10^{-3}$ mbar; 25 °C) for 2 h to remove toluene.

Surface Experiments. Electron induced surface reactions were studied by exposing nanometer thick films of HFeCo₃(CO)₁₂ under UHV conditions to electrons with a flood gun as the electron source. The electron induced surface reactions were monitored using XPS, while gas phase species were identified by MS. More details of the UHV chamber and its capabilities can be found in previous publications.^{46,47}

Sample Handling. To minimize any decomposition of the precursor caused by oxidation, the precursor molecules were loaded into a glass finger inside a N₂ glovebox and attached to a UHV compatible leak valve. The leak valve/glass finger assembly was then attached to the UHV chamber containing the XPS and MS. Due to the low volatility of HFeCo₃(CO)₁₂ (it volatilizes above 70 °C to provide a chamber pressure in the 10^{−7} Torr regime) we were able to evacuate the glass finger by directly pumping through the UHV leak valve with the compound at room temperature.

Substrate. All XPS and MS experiments were conducted on a polycrystalline gold substrate. Gold was chosen as the substrate, because it is chemically inert, and none of its XPS peaks overlap with those of the precursor (Fe, Co, C, or O). Prior to each experiment, the Au substrate was cleaned by sputtering with 4 keV Ar⁺ ions, and the substrate surface cleanliness was verified by XPS scans of the C(1s) and O(1s) regions.

Creating HFeCo₃(CO)₁₂ Films. To volatilize HFeCo₃(CO)₁₂, we heated the glass finger to ~ 75 °C. This caused the chamber pressure to increase from $\sim 7 \times 10^{-9}$ to $\sim 8 \times 10^{-7}$ Torr. Nanometer thick films of HFeCo₃(CO)₁₂ were created by depositing HFeCo₃(CO)₁₂ precursor molecules onto sputter cleaned gold substrates at low temperatures (−120 °C). Depositing HFeCo₃(CO)₁₂ films at −120 °C as opposed to the lowest substrate temperatures that could be attained (−160 °C) minimized the chance of adsorption from residual water in the UHV chamber and any toluene residual from the synthesis of HFeCo₃(CO)₁₂. To create sufficiently thick HFeCo₃(CO)₁₂ films, as judged by XPS, it was necessary to dose the precursor molecules continuously for 2 h. The thickness of the films were estimated by measuring the signal attenuation from the

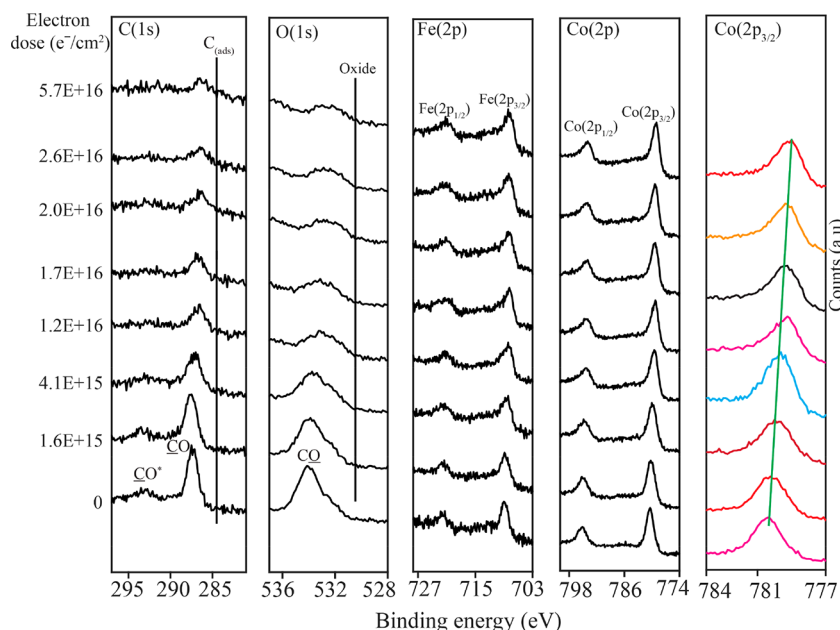


Figure 1. Evolution of the C(1s), O(1s), Fe(2p), Co(2p), and Co(2p_{3/2}) XPS regions of 1.4–1.6 nm thick HFeCo₃(CO)₁₂ films exposed to electron doses of $< \approx 5.7 \times 10^{16} \text{ e}^-/\text{cm}^2$. The C(1s), O(1s), Fe(2p), and Co(2p) spectra shown were measured with a pass energy of 22.36 eV; the RHS Co 2p_{3/2} region was followed with a pass energy of 11.2 eV.

substrate Au (4f) XPS peak, using an inelastic mean free path of 2 nm for Au (4f) photoelectrons.⁵³ Typical HFeCo₃(CO)₁₂ film thicknesses ranged from ~ 1.4 to ≈ 1.6 nm. Based on the effective size of the molecule (determined from the computed structure of the molecule⁴⁴), this corresponds to an average coverage of between 1 and 2 monolayers. Although films were deposited using a substrate temperature of -120 °C, we increased the substrate temperature from -120 to -60 °C prior to electron irradiation to ensure that any coadsorbed water had desorbed prior to electron irradiation.

Electron Source. A commercial flood gun (Spec FG 15/40) was used to irradiate the adsorbed precursor molecules. The electron flux was measured by recording the target current on the sample. During any one experiment, we maintained a constant electron flux on the surface/film by keeping the target current constant. Electron exposures were reported in terms of the electron dose (electron dose = target current \times electron exposure). For an electron dose of up to $5.6 \times 10^{16} \text{ e}^-/\text{cm}^2$, we typically used a target current of $5 \mu\text{A}$, while for larger electron doses, we used a target current of $30 \mu\text{A}$. For all experiments, we used an incident electron energy of 500 eV. This represents the sum of the electron energy from the flood gun (+480 V) and a positive bias (+20 V), which was applied to prevent the escape of secondary electrons generated by the primary electrons.

X-ray Photoelectron Spectroscopy. All XPS data was measured by PHI 5400 XPS using Mg K α X-rays ($h\nu = 1253.6$ eV). Spectra were deconvoluted using commercial software (CASA XPS). The binding energies for C(1s), O(1s), Fe(2p), and Co(2p) peaks were calibrated by aligning the Au (4f_{7/2}) peak to 84.0 eV. Unless noted, all XPS data were acquired at a pass energy of 22.36 eV, 0.125 eV/step, and 50 ms/step.

Mass Spectrometry. Gas phase species were monitored with a quadrupole mass spectrometer (Balzers Prisma QMS, 0–200 amu) located ~ 5 cm from the sample and operating in electron ionization mode (electron energy = 70 eV)

RESULTS

Figures 1 and 2 show the changes in the C(1s), O(1s), Fe(2p), and Co(2p) XPS regions that occur during the electron irradiation of nanometer thick films of HFeCo₃(CO)₁₂. Figure S1 shows that the X-ray irradiation of adsorbed HFeCo₃(CO)₁₂ films (needed for XPS analysis) produces a similar change to the C(1s) and O(1s) regions as that produced by 500 eV electrons. This similarity supports the idea that the dissociation

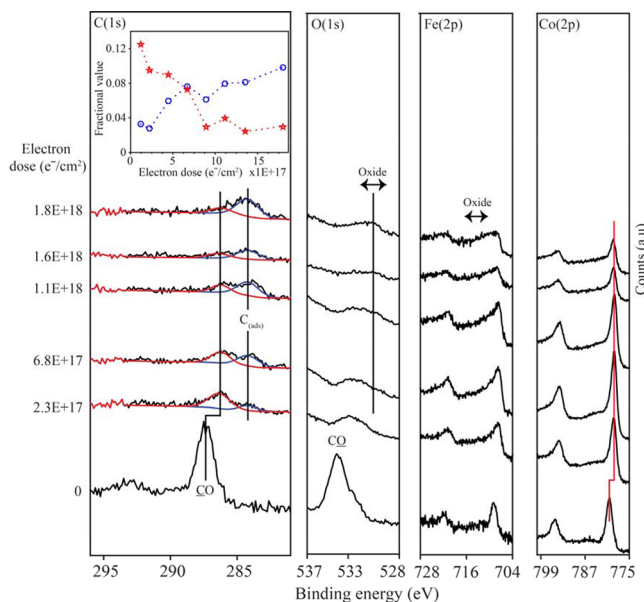


Figure 2. Evolution of the C(1s), O(1s), Fe(2p), and Co(2p) XPS regions of 1.4–1.6 nm thick HFeCo₃(CO)₁₂ films, exposed to an electron dose $> 2 \times 10^{17} \text{ e}^-/\text{cm}^2$. The inset in the C(1s) region shows the fractional change in the coverage of carbonyl (red stars) and graphitic carbon atoms (open blue circles) for these larger electron doses; carbon areas have been normalized to the XPS signal initially observed in the C(1s) region prior to any electron irradiation.

of adsorbed $\text{HFeCo}_3(\text{CO})_{12}$ precursor molecules is mediated by secondary electrons, in this case produced by X-ray irradiation of the Au substrate. The sensitivity of the $\text{HFeCo}_3(\text{CO})_{12}$ film toward secondary electrons produced by the X-rays was determined in a separate control experiment. Analysis of the rate of decrease in the O(1s) signal intensity produced by X-ray irradiation (Figure S2) reveals that the time taken for one XPS scan of the C(1s), O(1s), Fe(2p), and Co(2p) regions as shown in Figure 1 corresponds to an electron dose of $9.25 \times 10^{14} \text{ e}^-/\text{cm}^2$. To reflect this, the electron dose reported in this paper reflects the effective electron dose delivered by the electron gun and the X-ray irradiation. In practice, the effect of X-ray irradiation is only significant for cumulative electron doses $< \approx 2 \times 10^{15} \text{ e}^-/\text{cm}^2$.

Prior to electron irradiation, Figure 1 shows that the C(1s) XPS region consists of two peaks centered at 287.6 and 293.2 eV, both indicative of adsorbed carbonyl groups.^{54,55} The lower binding energy peak can be assigned to the C(1s) peak of the CO species, while the higher binding energy peak is a shake up feature caused by a $\pi-\pi^*$ transition that can accompany the ejection of C(1s) electrons in metal carbonyls.^{54,55} The O(1s) region also initially consists of two peaks: an asymmetric peak centered at 534.1 eV associated with the O(1s) peak of CO ligands and a weaker $\pi-\pi^*$ shake up peak centered at ~ 540 eV (not shown).^{54,55} The two peaks initially present within the Fe region at 709 and 722 eV correspond to Fe $2p_{3/2}$ and Fe $2p_{1/2}$ transitions, respectively. Similarly, the two peaks in the Co XPS region centered at 780.4 and 795.1 eV correspond to Co $2p_{3/2}$ and Co $2p_{1/2}$ transitions, respectively. It should also be noted that the C(1s), O(1s), Fe(2p), and Co(2p) XPS spectra shown in Figure 1 prior to electron exposure are consistent with the deposition of molecular $\text{HFeCo}_3(\text{CO})_{12}$. For example, the XPS spectral features in the C(1s) and O(1s) regions are due to the presence of carbonyl groups, and the cobalt to iron ratio determined from analysis of the Co(2p) and Fe(2p) regions is 3.19, close to the stoichiometric 3:1 ratio of the compound.

For electron doses $< \approx 5.7 \times 10^{16} \text{ e}^-/\text{cm}^2$, Figure 1 demonstrates that the dominant change is the significant decrease in the C(1s) and O(1s) peak areas. As a result, the $\pi-\pi^*$ shake up feature in the C(1s) region can no longer be detected for electron doses in excess of $\sim 2.6 \times 10^{16} \text{ e}^-/\text{cm}^2$. The peak positions in the C(1s) and O(1s) regions both shift to lower binding energy as the electron dose increases, although the shape of the peaks remains relatively unchanged. Furthermore, there is no sign of graphitic carbon or the formation of oxide species, evident by the absence of any graphitic carbon (C(1s) peak at ~ 284.5 eV) or oxide species (peak at ~ 530.5 eV). The fractional coverage of both carbon and oxygen atoms for an electron dose of $< 5.7 \times 10^{16} \text{ e}^-/\text{cm}^2$ follow the same trend, both decreasing by $\sim 75\%$ (shown as an inset to Figure 3a), while the C:O ratio remains constant. In contrast to the obvious changes in the C(1s) and O(1s) regions, the integrated areas of the peaks in the Fe(2p) and Co(2p) regions remain essentially constant (varying by less than 10%) as a result of electron irradiation, indicating an absence of any measurable metal desorption. Although the Fe(2p) peaks remain relatively unaffected, there is a slight broadening and a shift toward higher binding energy with increasing electron dose (total shift is ~ 0.23 eV). Due to the higher spectral intensity observed in the Co(2p) region, it was possible to follow the changes in this region with a higher energy resolution using a lower pass energy. Results of these experiments, shown in the right-hand side plot of Figure 1,

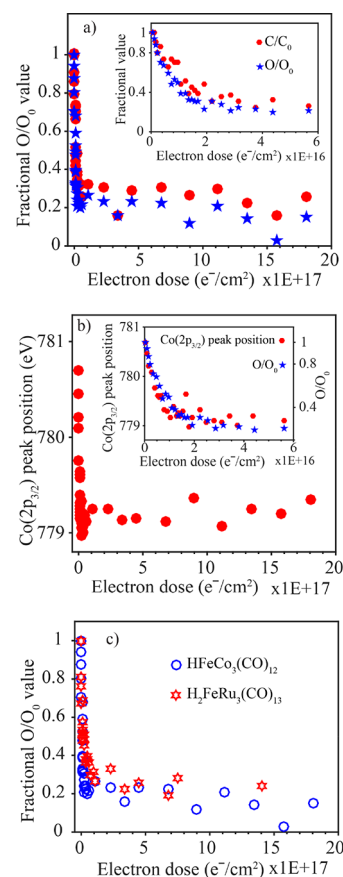


Figure 3. Change in (a) fractional coverage of carbon and oxygen atoms and (b) Co($2p_{3/2}$) peak position for 1.4–1.6 nm thick $\text{HFeCo}_3(\text{CO})_{12}$ films, as a function of electron dose. The insets in (a) and (b) show the corresponding changes to the fractional coverage of carbon and oxygen atoms as well as the Co($2p_{3/2}$) peak position for the comparatively small electron doses ($< 6 \times 10^{16} \text{ e}^-/\text{cm}^2$) shown in Figure 1. Figure 3c compares the change in fractional coverage of oxygen atoms for $\text{HFeCo}_3(\text{CO})_{12}$ and $\text{H}_2\text{FeRu}_3(\text{CO})_{13}$ films exposed to 500 eV electrons, both plotted as a function of electron dose ($\text{H}_2\text{FeRu}_3(\text{CO})_{13}$ data from ref 45).

indicate that increasing the electron dose to about $5.7 \times 10^{16} \text{ e}^-/\text{cm}^2$ leads to a small but measurable shift in the Co($2p_{3/2}$) peak position (total shift ≈ 1.3 eV) and a peak shape that becomes increasingly asymmetric. The change in the Co(2p) peak position for these comparatively small electron doses, shown as the inset to Figure 3b is seen to be closely correlated with the decrease in oxygen atom coverage (and therefore by inference also the coverage of carbon atoms).

Figure 2 shows the evolution of the C(1s), O(1s), Fe(2p), and Co(2p) XPS regions for significantly larger electron doses ($> 2 \times 10^{17} \text{ e}^-/\text{cm}^2$) than those shown in Figure 1. For comparative purposes, the spectra of a $\text{HFeCo}_3(\text{CO})_{12}$ film prior to electron irradiation is shown as the bottom most spectra. In marked contrast to the behavior observed for smaller electron doses (Figure 1), the integrated areas in both the C(1s) and O(1s) regions remains invariant for an electron dose $> 2 \times 10^{17} \text{ e}^-/\text{cm}^2$, as shown in Figure 3a. However, despite the lack of changes in area, there are changes in the spectral profiles in both the C(1s) and O(1s) regions. For example, there is a slow, but systematic, decrease in the carbonyl peak centered at 287.6 eV, accompanied by the concomitant appearance and subsequent increase in the intensity of a new peak centered at

284.5 eV, which can be ascribed to graphitic carbon (C_{ads}).⁵⁶ Indeed, Figure 2 shows that after an electron dose of $1.8 \times 10^{18} \text{ e}^-/\text{cm}^2$, the C(1s) region is dominated by spectral intensity from graphitic carbon, with almost no observable C signal from remaining CO. In the O(1s) region, these larger electron doses cause the peak to broaden and shift to lower binding energy with a peak at $\sim 530.5 \text{ eV}$ becoming increasingly prevalent. This new lower binding energy peak is consistent with the formation of an oxide; this assertion is supported by the observation of the same peak when a $\text{HFeCo}_3(\text{CO})_{12}$ film was exposed to an extremely large electron dose ($2.1 \times 10^{18} \text{ e}^-/\text{cm}^2$) in the presence of residual water vapor in the background (see Figure S3). The observation of oxide species in the O(1s) region is also coincident with a visible broadening of the Fe(2p) peak to higher binding energy, indicative of the formation of iron oxides. In contrast, there were no measurable changes in the Co(2p) XPS region, including the Co(2p_{3/2}) peak position (Figure 3b). Analysis of Figure 3 reveals that the changes to the C(1s), O(1s), and Fe(2p) regions observed in Figure 2 ($1.8 \times 10^{18} \text{ e}^-/\text{cm}^2 < \text{electron doses} > 2 \times 10^{17} \text{ e}^-/\text{cm}^2$) occur for electron doses that are at least an order of magnitude greater than those responsible for the changes in Figure 1 (electron doses $< 5.7 \times 10^{16} \text{ e}^-/\text{cm}^2$). Figure 3c shows that the fractional decrease in the coverage of oxygen atoms seen for $\text{HFeCo}_3(\text{CO})_{12}$ in this study is also very similar in magnitude and rate to the one observed for another recently studied bimetallic compound, $\text{H}_2\text{FeRu}_3(\text{CO})_{13}$,⁴⁵ during electron exposure.

Figure 4 compares mass spectra (0–100 amu) observed from (top) the gas phase $\text{HFeCo}_3(\text{CO})_{12}$ and (bottom) during the electron irradiation of

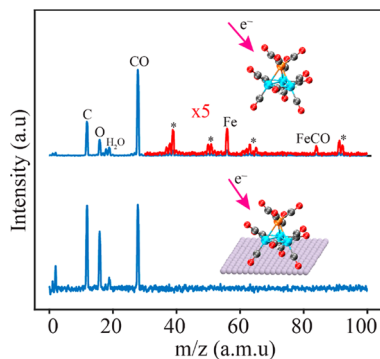


Figure 4. Mass spectrum (0–100 amu) of (top) gas phase $\text{HFeCo}_3(\text{CO})_{12}$ and (bottom) during the electron irradiation of a $\text{HFeCo}_3(\text{CO})_{12}$ film. No fragments were observed between 100–200 amu. The bottom spectrum represents the average of five mass spectra recorded during an electron dose of $3.2 \times 10^{16} \text{ e}^-/\text{cm}^2$.

electron irradiation of adsorbed $\text{HFeCo}_3(\text{CO})_{12}$ molecules. The most intense peaks observed in the mass spectrum of gas phase $\text{HFeCo}_3(\text{CO})_{12}$ were CO (28), C (12), and O (16), along with smaller peaks at Fe (56), FeCO (84), and water vapor residual in the UHV chamber. Peaks marked with a star originate from toluene, used in the synthesis of $\text{HFeCo}_3(\text{CO})_{12}$. During the electron beam irradiation of adsorbed $\text{HFeCo}_3(\text{CO})_{12}$ films, the only peaks observed were associated with CO (28, 12, and 16), along with a small contribution from residual water vapor. The absence of any discernible Fe or FeCO peaks supports the findings from the XPS (see Figures 1 and 2) that electron irradiation does not cause any desorption

of metal-containing fragments from adsorbed $\text{HFeCo}_3(\text{CO})_{12}$ molecules.

Figure 5 shows the normalized CO desorption kinetics observed during the electron irradiation of $\text{HFeCo}_3(\text{CO})_{12}$

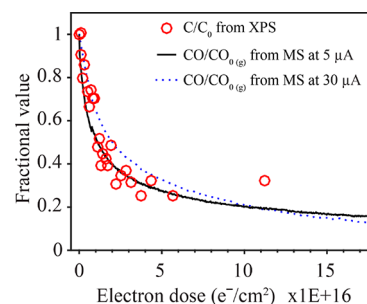


Figure 5. Kinetics of CO desorption observed during irradiation of 1.4–1.6 nm thick $\text{HFeCo}_3(\text{CO})_{12}$ film (monitored at $m/z = 12$ (C)), plotted as a function of electron dose at a target current of $5 \mu\text{A}$ (black solid line) and $30 \mu\text{A}$ (blue dotted line). Also shown is the fractional coverage of carbon atoms, determined by XPS data from Figure 1 (red circles).

films using two different target currents (5 and $30 \mu\text{A}$), plotted in terms of the total electron dose (electron dose = target current \times time). The CO desorption kinetics were monitored by following changes in the signal at $m/z = 12$ (C) which originates exclusively from CO. The rate of CO desorption from the film is observed to be greatest at the onset of irradiation and decreases to background levels once an electron dose of $\sim 3 \times 10^{16} \text{ e}^-/\text{cm}^2$ is reached. Moreover, the CO desorption kinetics for the two target currents, when plotted in terms of the total electron dose, are seen to be very similar to one another. Figure 5 also shows that the rate of CO desorption from the film is closely correlated with the rate of loss of carbon atoms (and therefore by inference oxygen atoms) from the films as observed by XPS.

Figure 6a shows the changes in the C(1s), O(1s), Fe(2p), and Co(2p) XPS regions that occur when a $\text{HFeCo}_3(\text{CO})_{12}$ film initially adsorbed at $-60 \text{ }^\circ\text{C}$ was exposed to an electron dose of $2.0 \times 10^{16} \text{ e}^-/\text{cm}^2$ and then subsequently annealed to RT ($25 \text{ }^\circ\text{C}$). An electron dose of $2.0 \times 10^{16} \text{ e}^-/\text{cm}^2$ was chosen, because it corresponds to the smallest electron dose required to cause all of the electron induced desorption of carbon and oxygen atoms from $\text{HFeCo}_3(\text{CO})_{12}$ films as determined by XPS (see Figure 3a). Changes in the C(1s) and O(1s) XPS regions after an electron dose of $2.0 \times 10^{16} \text{ e}^-/\text{cm}^2$ are similar to those reported in Figure 1, with a significant decrease in the C(1s) and O(1s) XPS peak areas. The uppermost spectra in Figure 6a show that upon annealing this electron irradiated film, all of the residual intensity in the C(1s) and O(1s) regions disappears, and only signal intensity in the metallic Co(2p) and Fe(2p) regions remains.

In Figure 6b, we compare the experiment shown in Figure 6a with the recent results of an analogous experiment conducted using $\text{H}_2\text{FeRu}_3(\text{CO})_{13}$.⁴⁵ In the case of $\text{H}_2\text{FeRu}_3(\text{CO})_{13}$, an electron dose of $1.3 \times 10^{17} \text{ e}^-/\text{cm}^2$ was found to be sufficient to complete the initial stage of reaction, where the O(1s) intensity was reduced by $\sim 70\%$ of its initial value (see Figure 3c). As discussed previously, this fractional decrease in the O(1s) signal is comparable to that observed in the present study of $\text{HFeCo}_3(\text{CO})_{12}$. However, upon annealing the irradiated $\text{H}_2\text{FeRu}_3(\text{CO})_{13}$ film to room temperature, it retains

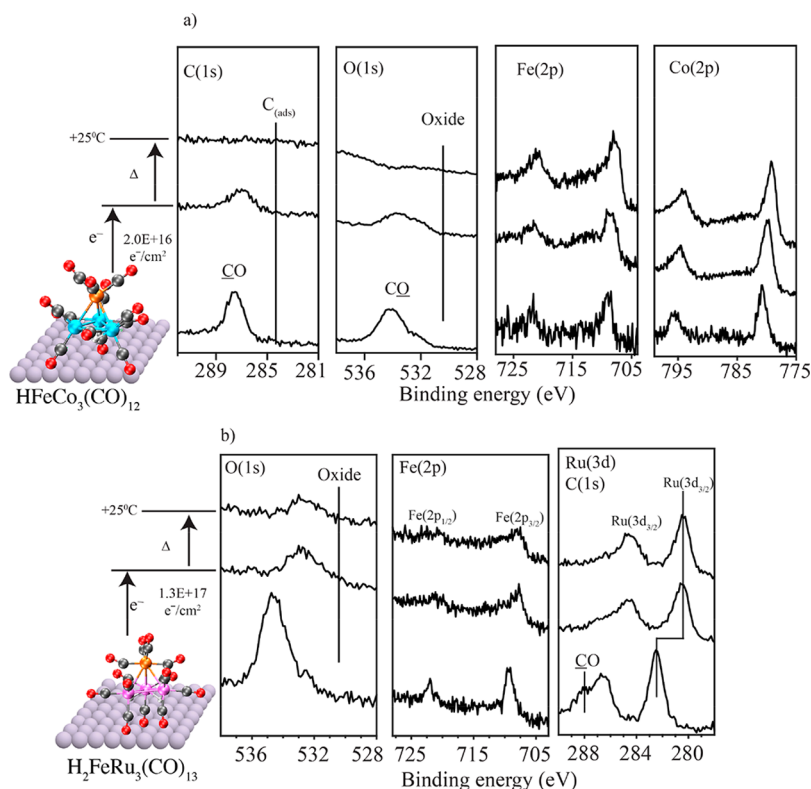


Figure 6. (a) Changes in the C(1s), O(1s), Fe(2p), and Co(2p) XPS regions when 1.4–1.6 nm thick HFeCo₃(CO)₁₂ film was exposed to an electron dose of 2.0×10^{16} e⁻/cm² (middle set of spectra) and then subsequently heated to room temperature (25 °C) (uppermost set of spectra); (b) changes in O(1s), Fe(2p), and Ru(3d)/C(1s) regions for a 1.1–1.4 nm thick H₂FeRu₃(CO)₁₃ film first irradiated to 1.3×10^{17} e⁻/cm² (middle set of spectra) and then annealed to RT (uppermost set of spectra), adapted from ref 45. For both molecules, the films were adsorbed on a gold surface.

measurable O(1s) intensity. This is in contrast to the loss of all O(1s) intensity for the irradiated HFeCo₃(CO)₁₂ film (compare the uppermost O(1s) spectra in Figure 6a and b).

DISCUSSION

Based on our XPS and MS measurements, the electron induced surface reactions of HFeCo₃(CO)₁₂ can be partitioned into two stages. In the first stage, which occurs for electron doses of $\approx 5.7 \times 10^{16}$ e⁻/cm², the transformation is dominated by significant decreases in the C(1s) and O(1s) XPS peak areas accompanied by CO desorption. The second stage of the reaction occurs for an electron dose $\approx 5.7 \times 10^{16}$ e⁻/cm². In this stage, the residual carbon and oxygen coverage remain almost constant, although changes do occur to the oxygen-, carbon-, and iron-containing species. In the following sections, we will discuss these two stages of the reaction and their relationship to the FEBID process in more detail.

First Step: Electron Stimulated CO Desorption/Precursor Deposition. The initial electron stimulated process leads to significant CO desorption from adsorbed HFeCo₃(CO)₁₂ molecules. Schematically, we can represent this step as shown in Figure 7

The loss of CO is observed directly by mass spectrometry in Figure 5, and it is CO desorption that is responsible for the loss of intensity in the O(1s) and C(1s) peak areas shown in Figures 1 and 3. The loss of CO is further supported by the observation in XPS that although the peak areas decrease, the O:C ratio remains constant. Moreover, the loss of carbon and oxygen observed by XPS is coincident with the rate of CO desorption (Figure 5). Analysis of the C(1s) and O(1s) regions

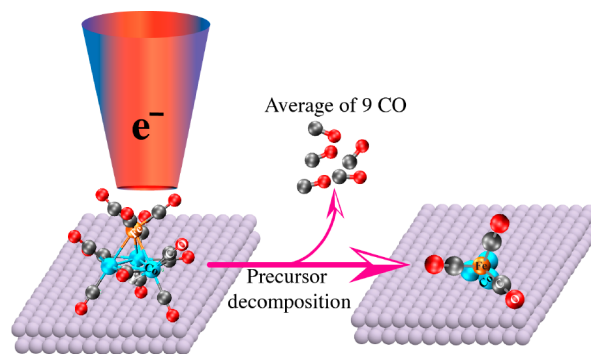


Figure 7. Schematic for electron induced dissociation of adsorbed HFeCo₃(CO)₁₂.

during this initial step also reveals an absence of any graphitic carbon or oxide species, indicating that CO desorption from the parent (precursor) occurs in the absence of CO decomposition. The extent of CO desorption can be determined by noting that during this initial stage of the reaction, the carbon and oxygen signals both decrease to $\sim 25\%$ of their initial values. Based on the stoichiometry of the precursor (HFeCo₃(CO)₁₂), this indicates that on average each precursor molecule loses 9 of its initial 12 CO ligands.

CO desorption from the precursor under the influence of electron irradiation would cause the adsorbed HFeCo₃(CO)₁₂ molecules to transform into partially decarbonylated species with an average stoichiometry of HFeCo₃(CO)₃ as shown in Figure 7. This loss of CO ligands as the precursor is

transformed into a partially decarbonylated intermediate is reflected in the increasingly asymmetric peak shape and decrease in binding energy in the Co ($2p_{3/2}$) peak from 780.4 to 779.1 eV (Figure 1), which is closer to the binding energy and asymmetric peak shape associated with metallic Co ($2p_{3/2}$ binding energy of 778.3 eV).⁵⁶ Consistent with this assertion, Figure 3 shows that the shift in the Co($2p_{3/2}$) peak position occurs concomitantly with the loss of C and O from the film. The significantly lower signal-to-noise (see Figure 1) prevented us from conducting the same detailed analysis in the Fe($2p$) region.

In separate experiments, we studied $\text{DFeCo}_3(\text{CO})_{12}$ in an attempt to probe the fate of the hydrogen atoms using mass spectrometry. However, the signal at mass 2 was dominated by contributions from residual H_2 in the UHV chamber, and the mass 4 signal from D_2 was inconsistent. Consequently, we are not able to make a definitive statement as to the fate of the hydrogen atom in the precursor, although in gas phase experiments, the hydrogen is found to stay attached to the metal atoms during electron exposure and fragmentation,⁴³ and we therefore presume the same is the case here.

In relationship to FEBID, this initial interaction of electrons with adsorbed $\text{HFeCo}_3(\text{CO})_{12}$ molecules corresponds to the event that will convert the molecular precursor into a nonvolatile, partially decarbonylated species, while the CO ligands lost from the precursor will be pumped away. This first step is analogous to reactions we have observed with other FEBID precursors like $\text{Co}(\text{CO})_3\text{NO}$ ⁵⁰ and $\text{W}(\text{CO})_6$,⁴⁹ characterized by partial ligand (CO) desorption. What is particularly noteworthy in this study is the extent of CO desorption; our results indicate that $\text{HFeCo}_3(\text{CO})_{12}$ loses on average 75% of its 12 CO ligands in the initial step. In contrast, no more than 50% of the CO groups in $\text{W}(\text{CO})_6$ and $\text{Co}(\text{CO})_3\text{NO}$ desorb when these FEBID precursors decompose under the influence of electron irradiation. In terms of the reaction cross section, we note that precursor decomposition is complete by $\sim 5 \times 10^{16} \text{ e}^-/\text{cm}^2$. This is similar to values we have measured before for other carbonyl precursors. For example, CO desorption from $\text{W}(\text{CO})_6$ and $\text{Co}(\text{CO})_3\text{NO}$ was complete after electron doses of $\sim 5 \times 10^{16} \text{ e}^-/\text{cm}^2$ and $6.2 \times 10^{16} \text{ e}^-/\text{cm}^2$. Thus, results from the present study add to the body of data suggesting that although the nature and extent of ligand desorption is precursor dependent, the rate of electron stimulated precursor decomposition is relatively constant.

In the UHV surface science studies, electron induced precursor dissociation takes place under the influence of a constant flux of electrons and in a pseudo precursor limited regime, since there is no supply of precursor molecules during electron irradiation. Under these conditions, the rate of CO loss should be modeled by first order kinetics as a function of the electron dose. Indeed, the initial loss of carbon and oxygen from the film, using the data shown in Figure 3a, can be well fit to an exponential decay yielding an average rate constant of $1.1 \times 10^{-16} \text{ e}^-/\text{cm}^2$. This corresponds to the total reaction cross section⁵⁷ for $\text{HFeCo}_3(\text{CO})_{12}$ molecules adsorbed on gold and exposed to 500 eV electrons ($\sigma(\text{HFeCo}_3(\text{CO})_{12})_{500 \text{ eV}} = 1.1 \times 10^{-16} \text{ e}^-/\text{cm}^2$). This value is comparable to the total reaction cross section for MeCpPtMe_3 ($\sigma(\text{MeCpPtMe}_3)_{500 \text{ eV}} = 2.2 \times 10^{-16} \text{ e}^-/\text{cm}^2$),⁴⁶ a common FEBID precursor.^{1,2}

The extent of CO desorption also provides a basis to identify the underlying mechanism responsible for the precursor's decomposition. In FEBID, it is widely accepted that the precursor molecules react with the secondary electrons

generated by the interaction of the primary beam with the substrate, rather than directly with the primary electron beam.^{34,35} In surface science studies, different electron stimulated decomposition mechanisms (e.g., DEA vs DI) cannot be differentiated, because precursor molecules are exposed simultaneously to secondary electrons with a wide range of energies, predominantly in the regime between 0 and 100 eV. However, this limitation does not exist in gas phase studies, where fragments are generated under single collision conditions when electrons of well-defined energies interact with precursor molecules. A recent gas phase study of the $\text{HFeCo}_3(\text{CO})_{12}$ molecule^{43–45} carried out using a crossed electron/molecule set up under single collision conditions has shown that an average of two to three CO ligands are lost per incident electron interaction from the molecule through DEA, while DI of $\text{HFeCo}_3(\text{CO})_{12}$ molecules at 70 eV leads to the average loss of four to nine CO ligands.⁴⁵ In these gas phase experiments, charged fragments are detected and the lower limit of CO loss for either process is calculated by assuming that the neutral fragment stays intact, while the upper limit presumes total CO loss from the neutral fragment for DI. For DEA the upper limit is calculated by assuming that all excess energy leads to further CO loss from the neutral, using a metal–CO bond energy of approximately 3eV. It is clear from the current surface experiments that metal-containing fragments are not desorbing from the surface. Thus, through comparison of the average CO loss in DEA and DI of $\text{HFeCo}_3(\text{CO})_{12}$ in the gas phase, with the initial CO loss observed here, it appears more likely that the initial electron induced dissociation of adsorbed $\text{HFeCo}_3(\text{CO})_{12}$ molecules proceeds through DI rather than DEA. Comparisons of gas phase and surface experiments of other organometallic FEBID precursors has indicated that some precursors react predominantly through DEA ($\text{MeCpPt}^{\text{IV}}\text{Me}_3$,^{46,58} $\text{Pt}(\text{PF}_3)_4$,^{48,59}), while others appear to be best described as a combination of DEA and DI processes ($\text{W}(\text{CO})_6$,^{49,60} $\text{Co}(\text{CO})_3\text{NO}$,^{50,61}). In contrast, the bimetallic $\text{HFeCo}_3(\text{CO})_{12}$ appears to decompose predominantly via DI. Similarly, another bimetallic precursor molecule $\text{H}_2\text{FeRu}_3(\text{CO})_{13}$ also appears to decompose through DI.⁴⁵ We however note that the extent of neutral dissociation is not known for these precursors. It should also be noted that in principle, surface induced dissociation of initially formed intermediates may occur and this would compromise direct comparisons between gas phase and surface science studies.⁶²

Gas phase studies can also be analyzed to determine the potential significance of metal–metal bond rupture during the initial decomposition of the bimetallic precursor. Indeed, metal–metal bond cleavage is significant in DI of $\text{HFeCo}_3(\text{CO})_{12}$.⁴⁵ The total branching ratio for metal–metal bond ruptures in DI is about 0.5, with $\text{Fe}(\text{CO})_n^+$ ($n = 0–5$) being the most significant species. In the UHV surface science approach employed in this study, MS and XPS data provide information on the average number of CO molecules desorbing and the resultant stoichiometric change in the $\text{HFeCo}_3(\text{CO})_{12}$ film. If we assume that CO ligands are lost from $\text{HFeCo}_3(\text{CO})_{12}$ via DI, then we are observing a statistical process where the adsorbates present after initial electron induced dissociation of $\text{HFeCo}_3(\text{CO})_{12}$ will be a mixture of partially decarbonylated species such as $\text{HFeCo}_3(\text{CO})_2$, $\text{HFeCo}_3(\text{CO})_3$, $\text{HFeCo}_3(\text{CO})_4$, and $\text{HFeCo}_3(\text{CO})_5$, etc., producing a film with an overall stoichiometry of $\text{HFeCo}_3(\text{CO})_3$. Examples of these intermediates are shown in Figures 7–10. However, it should be noted that these intermediates could include species where metal–

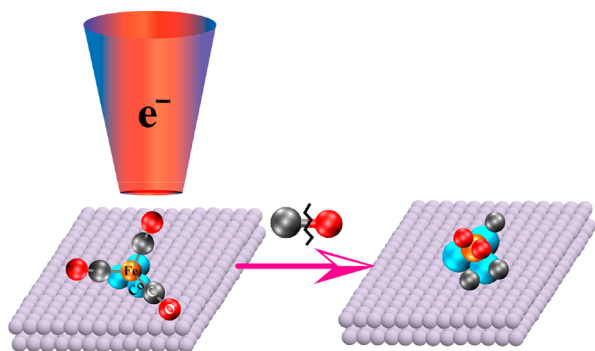


Figure 8. Schematic showing the electron stimulated CO decomposition of a partially decarbonylated $\text{HFeCo}_3(\text{CO})_{12}$ intermediate.

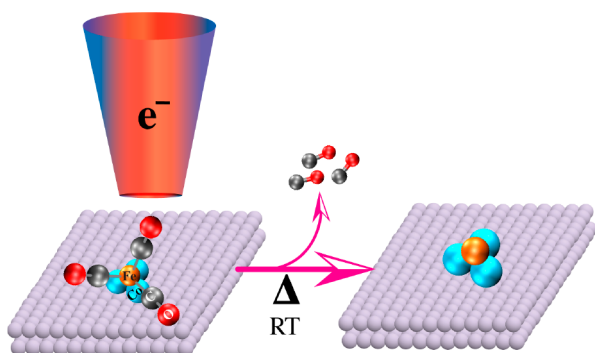


Figure 9. Effect of annealing a partially decarbonylated $\text{HFeCo}_3(\text{CO})_{12}$ intermediate to room temperature (RT), showing the resultant CO desorption.

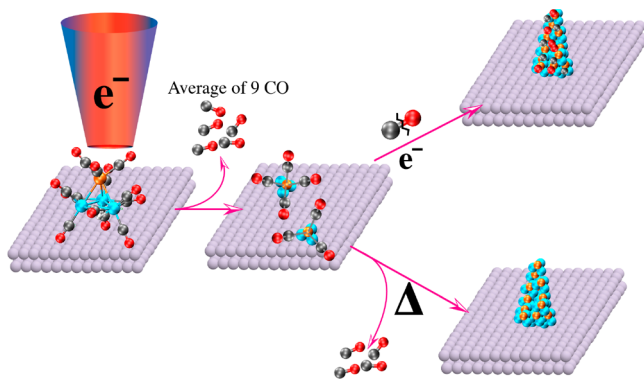
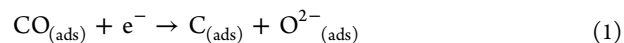


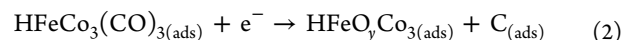
Figure 10. Schematic showing the electron induced decomposition of $\text{HFeCo}_3(\text{CO})_{12}$ and the competition between electron stimulated decomposition or thermal desorption of CO ligands from the partially decarbonylated intermediates produced by precursor decomposition.

metal bond cleavage also occurred during precursor decomposition (e.g., $\text{HFeCo}_3(\text{CO})_3$ could also include $\text{HFe}(\text{CO})_3$ and 3Co).

Second Step. (a). Electron Stimulated CO Decomposition. When CO desorption is complete at an electron dose of $\sim 5.7 \times 10^{16} \text{e}^-/\text{cm}^2$, the precursor $\text{HFeCo}_3(\text{CO})_{12}$ molecules have on average lost 9 of their 12 CO ligands and been converted into partially decarbonylated intermediates with an average stoichiometry of $\text{HFeCo}_3(\text{CO})_3$. Upon further increase in the electron dose ($> 5.7 \times 10^{16} \text{e}^-/\text{cm}^2$), the XPS data in Figure 2 indicate that the residual CO groups undergo electron stimulated decomposition, thus



This transformation is shown most clearly in the C(1s) region of Figure 2, where the decrease in the CO peak is accompanied by a concomitant increase in the coverage of $\text{C}_{(\text{ads})}$ species. Once an electron dose of $\sim 1.8 \times 10^{18} \text{e}^-/\text{cm}^2$ is reached, Figure 2 shows that the peak in the C(1s) region from the CO ligands has almost completely disappeared, and the $\text{C}_{(\text{ads})}$ peak dominates; this represents the conclusion of the electron stimulated reactions. Consistent with eq 1, there is no change in the integrated areas within either the C(1s) or O(1s) regions during this phase of the reaction. The formation of oxide species is most clearly evidenced by the formation of iron oxides, shown in Figure 2. Interestingly, there is no change in the Co(2p) peak profile, indicating that oxidation occurs exclusively to the iron atoms. The lack of any change in the O(1s) area in this second stage of the reaction also supports the idea that iron oxidation is exclusively a result of CO decomposition and not a result of reactions between iron atoms and oxygen-containing species in the vacuum chamber, a process that would be expected to increase the O(1s) signal intensity. Thus, the overall process of electron stimulated CO decomposition can be represented schematically by Figure 8 and by the reaction



The exclusivity of iron oxidation despite the presence of three times more Co atoms in the precursor also suggests that the residual CO ligands in the partially decarbonylated intermediates are bound predominantly and potentially exclusively to the lone Fe atom.

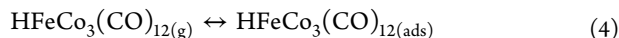
(b). Thermal Reactions. The overarching objective of this work is to better understand the elementary bond breaking reactions that occur during FEBID of the bimetallic precursor, $\text{HFeCo}_3(\text{CO})_{12}$. In FEBID, the initial deposition event must be induced by electron stimulated reactions with adsorbed precursor molecules; otherwise, nanostructures could not be directly written by the incident electron beam. However, once precursor deposition has occurred (the first stage in the reaction), any intermediates formed during the deposition step could be subject either to further electron stimulated reactions (part (a) above) or thermal reactions. However, in the present UHV surface science study, the partially decarbonylated intermediates are created at a substrate temperature of -60°C , while typical FEBID occurs at ambient temperatures. The relative importance and impact of any thermal reactions was therefore addressed by first exposing $\text{HFeCo}_3(\text{CO})_{12}$ molecules adsorbed at -60°C to an electron dose just sufficient to complete the first stage of reaction and create partially decarbonylated intermediates on the surface, before annealing these species to room temperature in the absence of any further electron irradiation. Results from these studies, shown in Figure 6a, demonstrate that almost all of the CO ligands remaining in the partially decarbonylated intermediate desorb when the substrate is annealed to room temperature, leaving behind only cobalt and iron atoms from the precursor molecule. The overall process is shown in Figure 9 and represented by the following equation



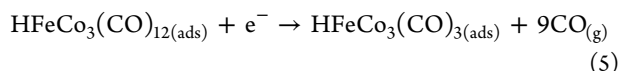
In this respect, the propensity for thermal desorption over thermal decomposition of the CO ligands in the partially

decarbonylated intermediates is in accord with the low levels (2–5%) of residual carbon and oxygen observed in conformal deposits created by the thermal dissociation of $\text{HFeCo}_3(\text{CO})_{12}$ at 200 °C.²¹

Overall Relationship between UHV Surface Science Data and FEBID. In FEBID of $\text{HFeCo}_3(\text{CO})_{12}$, the initial event is adsorption of precursor molecules onto the surface



The next step involves precursor decomposition, analogous to the first step identified in the present study (see Figure 7), which we have shown involves a single electron process leading to extensive CO desorption and the formation of a surface bound, partially decarbonylated intermediate, most likely through dissociative ionization of the parent molecule, thus



At this stage of FEBID, the partially decarbonylated intermediates thus formed can undergo one of two processes; further electron stimulated reactions, which can lead to decomposition of the residual CO ligands (see Figure 8)



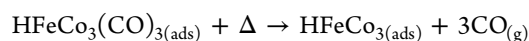
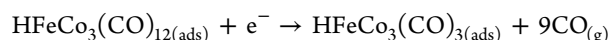
or thermal reactions initiating further CO desorption as shown in Figure 6a and schematically in Figure 9



The initial decomposition step as well as the subsequent competition between electron stimulated decomposition or thermal desorption of residual CO groups in the partially decarbonylated intermediates is shown schematically in Figure 10.

In a typical FEBID experiment, deposition is occurring under steady-state conditions in the presence of a constant flux of precursor molecules and electrons. Under these conditions, the fate of the $\text{HFeCo}_3(\text{CO})_3$ intermediates produced by the decomposition of the precursor will depend on the relative rates of the electron and thermally stimulated reactions (eqs 6 and 7 above). Although our UHV experiments do not provide a direct measure of these relative rates, we note that the rate of electron stimulated decomposition for the partially decarbonylated intermediates (step 2) is significantly slower than that of the initial electron stimulated decomposition of the parent $\text{HFeCo}_3(\text{CO})_{12}$ molecule (step 1). Thus, step 1 requires an electron dose $\sim 6 \times 10^{16} \text{ e}^-/\text{cm}^2$, while the electron stimulated decomposition of the resultant decarbonylated intermediate is only complete after an electron dose of $>1 \times 10^{18} \text{ e}^-/\text{cm}^2$. The relative inefficiency of electron stimulated decomposition of the $\text{HFeCo}_3(\text{CO})_3$ (s) intermediates (step 2) is most clearly evidenced in Figure 2 where XPS analysis shows that after an electron dose of $\sim 5.7 \times 10^{16} \text{ e}^-/\text{cm}^2$, all of the precursor molecules have decomposed, and yet, the adsorbate layer shows no evidence of any CO decomposition, as evidenced by the lack of any C_{ads} or oxide species. In contrast, if the rate of electron stimulated decomposition of the $\text{HFeCo}_3(\text{CO})_{3(\text{ads})}$ intermediate was occurring at a similar rate to the electron stimulated decomposition of the $\text{HFeCo}_3(\text{CO})_{12(\text{ads})}$ parent molecules, we would expect to see evidence of some C_{ads} and oxide species at a point in the reaction coordinate where all of the parent molecules have decomposed. This relative inefficiency of the electron stimulated decomposition of the partially decarbony-

lated $\text{HFeCo}_3(\text{CO})_3(\text{s})$ species (step 2) as compared to the initial precursor decomposition (step 1) suggests that once the partially decarbonylated intermediates are produced, thermal reactions are likely to play an important role in determining their ultimate fate. Under these conditions, the overall reactivity of the $\text{HFeCo}_3(\text{CO})_{12}$ precursor will be dominated by the following sequence of elementary reaction steps (eq 5 followed by eq 7, shown schematically by the lower reaction pathway in Figure 7)



In qualitative agreement with this mechanism of reaction, FEBID deposits created from $\text{HFeCo}_3(\text{CO})_{12}$ have been shown to exhibit metal contents $>80\%$, indicative of a process where further reactions of intermediate species are dominated by thermal desorption of residual ligands as opposed to electron stimulated decomposition.

Another difference between the present study and typical FEBID experiments is the energy of the primary electrons. In the present study, 500 eV primary electrons are used, while in FEBID, the incident electron energies are typically $>5 \text{ keV}$. It is widely accepted that the low energy secondary electrons ($>100 \text{ eV}$) generated by the interaction of the primary beam with the substrate are responsible for the electron induced chemistry.⁶³ However, although the primary electron energy (500 eV) is significantly lower than that used in FEBID (typically $>5 \text{ keV}$), the secondary electron energy distributions that have been reported are very similar.^{64,65}

Contrasting $\text{HFeCo}_3(\text{CO})_{12}$ with Other FEBID Precursors. In a recent publication, we have discussed gas phase fragmentation, electron induced surface reactions, and FEBID of the similar precursor $\text{H}_2\text{FeRu}_3(\text{CO})_{13}$.⁴⁵ Interestingly, the extent of CO desorption from $\text{HFeCo}_3(\text{CO})_{12}$ and $\text{H}_2\text{FeRu}_3(\text{CO})_{13}$ during the initial electron stimulated decomposition of these two bimetallic precursors is similar. For $\text{H}_2\text{FeRu}_3(\text{CO})_{13}$, the fractional decrease in the O(1s) signal indicates that on average 8–9 of the 13 CO ligands desorb, supported by MS data as well as changes in both the O(1s) and C(1s) regions.⁴⁵ This is comparable to the average loss of 9 CO groups from $\text{HFeCo}_3(\text{CO})_{12}$ during decomposition.

Despite this similarity, however, FEBID deposits made from $\text{HFeCo}_3(\text{CO})_{12}$ have metal contents $>80\%$, while FEBID deposits made from $\text{H}_2\text{FeRu}_3(\text{CO})_{13}$ have metal contents $<30\%$.⁴⁵ The root cause for the different performance of $\text{HFeCo}_3(\text{CO})_{12}$ and $\text{H}_2\text{FeRu}_3(\text{CO})_{13}$ in FEBID is clearly not a consequence of the efficiency of CO desorption in the initial electron induced dissociation process.

The difference in the behavior between these two precursors in FEBID appears to lie in the relative thermal stability of the CO groups within the partially decarbonylated intermediates created when the precursors decompose. Accordingly, Figure 6 demonstrates that while all of the CO groups in the $\text{HFeCo}_3(\text{CO})_3$ intermediate are thermally unstable with respect to desorption at room temperature, a significant fraction of the CO groups in the $\text{H}_2\text{FeRu}_3(\text{CO})_x$ ($x \approx 4,5$) intermediates are stable at room temperature and can therefore become incorporated into the deposit as it grows during FEBID.⁴⁵ This comparison supports our assertion that the second step, the thermal desorption of the intact CO groups from the initially created $\text{HFeCo}_3(\text{CO})_x$ ($x_{\text{avg}} \approx 3$) intermediates at

room temperature, is critical for the formation of the high metal content deposits achieved in FEBID with $\text{HFeCo}_3(\text{CO})_{12}$.

The performance of $\text{HFeCo}_3(\text{CO})_{12}$ as a FEBID precursor can also be compared with other CO-containing precursors we have studied under UHV surface science conditions, notably $\text{W}(\text{CO})_6$ ⁴⁹ and $\text{Co}(\text{CO})_3\text{NO}$.⁵⁰ For $\text{W}(\text{CO})_6$, the initial decomposition step is comparatively inefficient compared to $\text{HFeCo}_3(\text{CO})_{12}$, with less than 50% of the CO groups desorbing. Moreover, the residual partially decarbonylated $\text{W}(\text{CO})_x$ ($x \approx 4$) intermediates formed as a result of $\text{W}(\text{CO})_6$ decomposition are stable at room temperature and undergo efficient electron stimulated decomposition ($\text{W}(\text{CO})_x + e^- \rightarrow (\text{W}_x\text{O}_y)\text{C}$). Consequently, FEBID deposits produced from $\text{W}(\text{CO})_6$ contain oxidized tungsten atoms encased in a carbonaceous matrix.⁴⁹ In the case of $\text{Co}(\text{CO})_3\text{NO}$, initial decomposition leads to a desorption/loss of $\sim 50\%$ of the CO groups, although the residual CO groups thermally desorb when the substrate has reached 25 °C.⁵⁰ Consequently, FEBID deposits made from $\text{Co}(\text{CO})_3\text{NO}$ contain little or no carbon but are compromised in terms of metal content by the decomposition of the NO ligand, which occurs during electron stimulated decomposition of the precursor.^{66,67}

Results from the present study also show evidence of iron oxidation in the absence of any Co oxidation, suggesting that the residual CO ligands left over after the initial decomposition/deposition step are localized on the Fe and that the Co atoms are largely free of CO ligands. This would also be consistent with the importance of the apex ($\text{Fe}(\text{CO})_4^-$) loss channel observed in the gas phase studies⁴⁴ as well as the shift of the Co $2p_{3/2}$ peak position and its shape in the UHV surface science studies to one that is more indicative of metallic Co. Indeed, in a broader sense, if the results from the present study on $\text{HFeCo}_3(\text{CO})_{12}$, which are considered alongside the previously reported behavior of $\text{W}(\text{CO})_6$,^{68–70} $\text{Co}(\text{CO})_3\text{NO}$,^{66,67,71} $\text{H}_2\text{FeRu}_3(\text{CO})_{13}$,⁴⁵ and the high metal contents often observed from deposits made from $\text{Co}_2(\text{CO})_8$,^{32,72,73} the implication is that CO groups attached to cobalt atoms are efficiently removed in FEBID. The underlying reason for this apparent correlation is unclear and certainly worthy of further investigation. Another implication from this study and a comparison with other related studies is that precursors that yield deposits with relatively high metal content in FEBID are those where $>50\%$ of the native ligands desorb in the initial decomposition step to create intermediates whose ligands are themselves unstable with respect to thermal desorption. In this regard, a more detailed understanding including theoretical insights into the ligand bond strengths in FEBID intermediates, such as the partially decarbonylated intermediates implicated in the present study, would be invaluable in helping to rationalize our experimental observations and to provide predictive information for designing new FEBID precursors that yield deposits with high metal contents.

CONCLUSIONS

The reactions of electrons with physisorbed $\text{HFeCo}_3(\text{CO})_{12}$ molecules causes extensive CO loss, with an average of 9 CO molecules desorbing per molecule. This one electron process converts the organometallic precursor into partially decarbonylated nonvolatile intermediates with an average stoichiometry of $\text{HFeCo}_3(\text{CO})_3$. A comparison with related gas phase studies suggests that this initial electron induced CO desorption step is triggered by dissociative ionization of $\text{HFeCo}_3(\text{CO})_{12}$, rather than dissociative electron attachment. Although the rate of

electron stimulated decomposition is comparable to that of other CO-containing FEBID precursors that have been studied, e.g., $\text{W}(\text{CO})_6$ and $\text{Co}(\text{CO})_3\text{NO}$, the extent of CO desorption is significantly higher. Another recently studied bimetallic FEBID precursor ($\text{H}_2\text{FeRu}_3(\text{CO})_{13}$)⁴⁵, however, shows similarly extensive CO desorption. Further electron irradiation of the partially decarbonylated intermediate formed by the initial electron stimulated fragmentation of $\text{HFeCo}_3(\text{CO})_{12}$ causes decomposition of the residual CO ligands rather than further CO desorption, leading exclusively to Fe oxidation. This suggests that the CO groups in the partially decarbonylated intermediates are located primarily on the iron and not the Co atoms, further implying that the CO desorption observed during decomposition of the precursor occurs predominantly to the CO groups bound to the Co atoms. In contrast to the effect of electron irradiation, when the partially decarbonylated $\text{HFeCo}_3(\text{CO})_3$ intermediates are annealed to room temperature, complete CO desorption occurs, leaving behind only Fe and Co. These observations provide a means to rationalize the high metal contents observed when $\text{HFeCo}_3(\text{CO})_{12}$ is used in FEBID, with an overall reaction sequence that involves extensive CO desorption in the initial deposition step ($\text{HFeCo}_3(\text{CO})_{12(\text{ads})} + e^- \rightarrow \text{HFeCo}_3(\text{CO})_{3(\text{ads})} + 9\text{CO}_{(\text{g})}$), followed by thermal desorption of CO ligands from the resultant partially decarbonylated intermediate ($\text{FeCo}_3(\text{CO})_{3(\text{ads})} + \Delta \rightarrow \text{FeCo}_{3(\text{ads})} + 3\text{CO}_{(\text{g})}$).

ASSOCIATED CONTENT

Supporting Information

The Supporting Information is available free of charge on the ACS Publications website at DOI: 10.1021/acs.jpcc.7b08611.

Change in the C(1s) and O(1s) XPS region of $\text{HFeCo}_3(\text{CO})_{12}$ film when exposed to X-rays ($\text{Mg K}\alpha = 1253.6$ eV) (Figure S1); Comparing the change in O(1s) XPS peak area of $\text{HFeCo}_3(\text{CO})_{12}$ film during the X-ray irradiation with that during the 5 uA electron irradiation (Figure S2); O(1s) XPS scan for $\text{HFeCo}_3(\text{CO})_{12}$ film exposed to electron dose of 2.1×10^{18} e⁻/cm² in the presence of residual water (Figure S3) (PDF)

AUTHOR INFORMATION

Corresponding Author

*E-mail: howardf@jhu.edu (D.H.F.)

ORCID

Sven Barth: 0000-0003-3900-2487

Oddur Ingolfsson: 0000-0002-7100-9438

D. Howard Fairbrother: 0000-0003-4405-9728

Notes

The authors declare no competing financial interest.

ACKNOWLEDGMENTS

The authors acknowledge the support provided by the COST Action CELINA CM1301. D.H.F. thanks the National Science Foundation for support of this work through the linked collaborative grants CHE-1607621 and CHE-160754. O.I. acknowledges support from the Icelandic Center of Research (RANNIS) Grant No. 13049305(1-3) and the University of Iceland Research Fund. RKTP acknowledges a doctoral grant from the University of Iceland Research Fund and financial

support from the COST Action CM1301; CELINA, for short term scientific missions (STSMs) to enable this work.

REFERENCES

- (1) Utke, I.; Hoffmann, P.; Melngailis, J. Gas-assisted focused electron beam and ion beam processing and fabrication. *J. Vac. Sci. Technol. B* **2008**, *26*, 1197–1276.
- (2) Van Dorp, W.; Hagen, C. A critical literature review of focused electron beam induced deposition. *J. Appl. Phys.* **2008**, *104*, 081301.
- (3) Lepore, A. Electron-Beam ULSI Applications. In *Handbook of VLSI Microlithography*, 2nd ed.; Helbert, J., Ed.; William Andrew: New York, 2001; pp 670–755.
- (4) Bakshi, V., Ed. *EUV lithography*. SPIE: Bellingham, WA, 2008; Vol. PM178SC.
- (5) Edinger, K.; Becht, H.; Bihl, J.; Boegli, V.; Budach, M.; Hofmann, T.; Koops, H. W.; Kuschnerus, P.; Oster, J.; Spies, P.; et al. Electron-beam-based photomask repair. *J. Vac. Sci. Technol., B: Microelectron. Process. Phenom.* **2004**, *22*, 2902–2906.
- (6) Liang, T.; Frendberg, E.; Lieberman, B.; Stivers, A. Advanced photolithographic mask repair using electron beams. *J. Vac. Sci. Technol., B: Microelectron. Process. Phenom.* **2005**, *23*, 3101–3105.
- (7) Liang, T.; Stivers, A. R. Damage-free mask repair using electron-beam-induced chemical reactions. Proceedings of SPIE's 27th Annual International Symposium on Microlithography, Santa Clara, CA; SPIE: Bellingham, WA, 2002; pp 375–384.
- (8) Hubner, B.; Koops, H.; Pagnia, H.; Sotnik, N.; Urban, J.; Weber, M. Tips for scanning tunneling microscopy produced by electron-beam-induced deposition. *Ultramicroscopy* **1992**, *42-44*, 1519–1525.
- (9) Liu, Z.; Mitsuishi, K.; Furuya, K. The growth behavior of self-standing tungsten tips fabricated by electron-beam-induced deposition using 200 keV electrons. *J. Appl. Phys.* **2004**, *96*, 3983–3986.
- (10) Brown, J.; Kocher, P.; Ramanujan, C. S.; Sharp, D. N.; Torimitsu, K.; Ryan, J. F. Electrically conducting, ultra-sharp, high aspect-ratio probes for AFM fabricated by electron-beam-induced deposition of platinum. *Ultramicroscopy* **2013**, *133*, 62–66.
- (11) Chen, I.-C.; Chen, L.-H.; Ye, X.-R.; Daraio, C.; Jin, S.; Orme, C. A.; Quist, A.; Lal, R. Extremely sharp carbon nanocone probes for atomic force microscopy imaging. *Appl. Phys. Lett.* **2006**, *88*, 153102.
- (12) Graells, S.; Alcubilla, R.; Badenes, G.; Quidant, R. Growth of plasmonic gold nanostructures by electron beam induced deposition. *Appl. Phys. Lett.* **2007**, *91*, 121112.
- (13) Koops, H.; Hoinkis, O.; Honsberg, M.; Schmidt, R.; Blum, R.; Bottger, G.; Kuligk, A.; Liguda, C.; Eich, M. Two-dimensional photonic crystals produced by additive nanolithography with electron beam-induced deposition act as filters in the infrared. *Microelectron. Eng.* **2001**, *57-58*, 995–1001.
- (14) Weber-Bargioni, A.; Schwartzberg, A.; Schmidt, M.; Harteneck, B.; Ogletree, D.; Schuck, P.; Cabrini, S. Functional plasmonic antenna scanning probes fabricated by induced-deposition mask lithography. *Nanotechnology* **2010**, *21*, 065306.
- (15) Che, R.; Takeguchi, M.; Shimojo, M.; Zhang, W.; Furuya, K. Fabrication and electron holography characterization of FePt alloy nanorods. *Appl. Phys. Lett.* **2005**, *87*, 223109.
- (16) Winhold, M.; Schwalb, C. H.; Porrati, F.; Sachser, R.; Frangakis, A. S.; Kampken, B.; Terfort, A.; Auner, N.; Huth, M. Binary Pt–Si nanostructures prepared by focused electron-beam-induced deposition. *ACS Nano* **2011**, *5*, 9675–9681.
- (17) Porrati, F.; Begun, E.; Winhold, M.; Schwalb, C. H.; Sachser, R.; Frangakis, A.; Huth, M. Room temperature L10 phase transformation in binary CoPt nanostructures prepared by focused-electron-beam-induced deposition. *Nanotechnology* **2012**, *23*, 185702.
- (18) Porrati, F.; Kampken, B.; Terfort, A.; Huth, M. Fabrication and electrical transport properties of binary Co-Si nanostructures prepared by focused electron beam-induced deposition. *J. Appl. Phys.* **2013**, *113*, 053707.
- (19) Porrati, F.; Pohlitz, M.; Muller, J.; Barth, S.; Biegger, F.; Gspan, C.; Plank, H.; Huth, M. Direct writing of CoFe alloy nanostructures by focused electron beam induced deposition from a heteronuclear precursor. *Nanotechnology* **2015**, *26*, 475701.
- (20) Chini, P.; Colli, L.; Peraldo, M. *Gazz. Chim. Ital* **1960**, *90*, 1005–1019.
- (21) Boyd, E. P.; Ketchum, D. R.; Deng, H.; Shore, S. G. Chemical vapor deposition of metallic thin films using homonuclear and heteronuclear metal carbonyls. *Chem. Mater.* **1997**, *9*, 1154–1158.
- (22) Liu, D. K.; Lai, A. L.; Chin, R. J. Photochemical vapor deposition of mixed-metal thin films from organometallic precursors containing heteronuclear metal-metal bonds. *Mater. Lett.* **1991**, *10*, 318–322.
- (23) Lubbe, A. S.; Alexiou, C.; Bergemann, C. Clinical applications of magnetic drug targeting. *J. Surg. Res.* **2001**, *95*, 200–206.
- (24) Gazeau, F.; Baravian, C.; Bacri, J.-C.; Perzynski, R.; Shliomis, M. Energy conversion in ferrofluids: Magnetic nanoparticles as motors or generators. *Phys. Rev. E: Stat. Phys., Plasmas, Fluids, Relat. Interdiscip. Top.* **1997**, *56*, 614.
- (25) Childress, J. R.; Fontana, R. E. Magnetic recording read head sensor technology. *C. R. Phys.* **2005**, *6*, 997–1012.
- (26) Fernandez-Pacheco, A.; Streubel, R.; Fruchart, O.; Hertel, R.; Fischer, P.; Cowburn, R. P. Three-dimensional nanomagnetism. *Nat. Commun.* **2017**, *8*, 15756.
- (27) Silvis-Cividjian, N.; Hagen, C.; Kruit, P. Spatial resolution limits in electron-beam-induced deposition. *J. Appl. Phys.* **2005**, *98*, 084905.
- (28) Mulders, J. Practical precursor aspects for electron beam induced deposition. *Nanofabrication* **2014**, *1*, 74–79.
- (29) Lau, Y.; Chee, P.; Thong, J.; Ng, V. Properties and applications of cobalt-based material produced by electron-beam-induced deposition. *J. Vac. Sci. Technol., A* **2002**, *20*, 1295–1302.
- (30) Schoßler, C.; Kaya, A.; Kretz, J.; Weber, M.; Koops, H. Electrical and field emission properties of nanocrystalline materials fabricated by electron-beam induced deposition. *Microelectron. Eng.* **1996**, *30*, 471–474.
- (31) Rotkina, L.; Lin, J.-F.; Bird, J. Nonlinear current-voltage characteristics of Pt nanowires and nanowire transistors fabricated by electron-beam deposition. *Appl. Phys. Lett.* **2003**, *83*, 4426–4428.
- (32) Fernandez-Pacheco, A.; De Teresa, J.; Cordoba, R.; Ibarra, M. R. Magnetotransport properties of high-quality cobalt nanowires grown by focused-electron-beam-induced deposition. *J. Phys. D: Appl. Phys.* **2009**, *42*, 055005.
- (33) Pierson, H. O. *Handbook of chemical vapor deposition: principles, technology and applications*. William Andrew: New York, 1999.
- (34) Botman, A.; De Winter, D.; Mulders, J. Electron-beam-induced deposition of platinum at low landing energies. *J. Vac. Sci. Technol. B* **2008**, *26*, 2460–2463.
- (35) Silvis-Cividjian, N.; Hagen, C.; Leunissen, L.; Kruit, P. The role of secondary electrons in electron-beam-induced-deposition spatial resolution. *Microelectron. Eng.* **2002**, *61-62*, 693–699.
- (36) Thorman, R. M.; T P, R. K.; Fairbrother, D. H.; Ingolfsson, O. The role of low-energy electrons in focused electron beam induced deposition: four case studies of representative precursors. *Beilstein J. Nanotechnol.* **2015**, *6*, 1904–1926.
- (37) Ingolfsson, O.; Weik, F.; Illenberger, E. The reactivity of slow electrons with molecules at different degrees of aggregation: gas phase, clusters and condensed phase. *Int. J. Mass Spectrom. Ion Processes* **1996**, *155*, 1–68.
- (38) Bald, I.; Langer, J.; Tegeder, P.; Ingolfsson, O. From isolated molecules through clusters and condensates to the building blocks of life. *Int. J. Mass Spectrom.* **2008**, *277*, 4–25.
- (39) Bohler, E.; Warneke, J.; Swiderek, P. Control of chemical reactions and synthesis by low-energy electrons. *Chem. Soc. Rev.* **2013**, *42*, 9219–9231.
- (40) Christophorou, L. G., Ed. *Electron-Molecule Interactions and their Applications*; Academic Press: Orlando, FL, 1984.
- (41) Arumainayagam, C. R.; Lee, H.-L.; Nelson, R. B.; Haines, D. R.; Gunawardane, R. P. Low-energy electron-induced reactions in condensed matter. *Surf. Sci. Rep.* **2010**, *65*, 1–44.
- (42) Fabrikant, I. I.; Eden, S.; Mason, N. J.; Fedor, J. Recent Progress in Dissociative Electron Attachment: From Diatomics to Biomolecules. In *Advances In Atomic, Molecular, and Optical Physics*; Yelin, S.,

Arimondo, E., Lin, C., Eds.; Academic Press: Cambridge, MA, 2017; Vol. 66, pp 545–657.

(43) T P, R. K.; Bjornsson, R.; Barth, S.; Ingolfsson, O. Formation and decay of negative ion states up to 11 eV above the ionization energy of the nanofabrication precursor $\text{HFeCo}_3(\text{CO})_{12}$. *Chem. Sci.* **2017**, *8*, 5949–5952.

(44) T P, R. K.; Barth, S.; Bjornsson, R.; Ingolfsson, O. Structure and energetics in dissociative electron attachment to $\text{HFeCo}_3(\text{CO})_{12}$. *Eur. Phys. J. D* **2016**, *70*, 163.

(45) T P, R. K.; Weirich, P.; Hrachowina, L.; Hanefeld, M.; Bjornsson, R.; Hrodmarsson, H. R.; Barth, S.; Fairbrother, D. H.; Huth, M.; Ingolfsson, O. Electron Interactions with the heteronuclear carbonyl precursor ($\text{H}_2\text{FeRu}_3(\text{CO})_{13}$): from fundamental gas phase and surface science studies to focused electron beam induced deposition, in press.

(46) Wnuk, J. D.; Gorham, J. M.; Rosenberg, S. G.; van Dorp, W. F.; Madey, T. E.; Hagen, C. W.; Fairbrother, D. H. Electron induced surface reactions of the organometallic precursor trimethyl (methylcyclopentadienyl) platinum (IV). *J. Phys. Chem. C* **2009**, *113*, 2487–2496.

(47) Wnuk, J. D.; Gorham, J. M.; Rosenberg, S. G.; van Dorp, W. F.; Madey, T. E.; Hagen, C. W.; Fairbrother, D. H. Electron beam irradiation of dimethyl-(acetylacetonate) gold (III) adsorbed onto solid substrates. *J. Appl. Phys.* **2010**, *107*, 054301.

(48) Landheer, K.; Rosenberg, S. G.; Bernau, L.; Swiderek, P.; Utke, I.; Hagen, C. W.; Fairbrother, D. H. Low-energy electron-induced decomposition and reactions of adsorbed Tetrakis (trifluorophosphine) platinum [Pt (PF₃)₄]. *J. Phys. Chem. C* **2011**, *115*, 17452–17463.

(49) Rosenberg, S. G.; Barclay, M.; Fairbrother, D. H. Electron induced reactions of surface adsorbed tungsten hexacarbonyl (W (CO)₆). *Phys. Chem. Chem. Phys.* **2013**, *15*, 4002–4015.

(50) Rosenberg, S. G.; Barclay, M.; Fairbrother, D. H. Electron beam induced reactions of adsorbed cobalt tricarbonyl nitrosyl (Co (CO)₃NO) molecules. *J. Phys. Chem. C* **2013**, *117*, 16053–16064.

(51) Spencer, J. A.; Brannaka, J. A.; Barclay, M.; McElwee-White, L.; Fairbrother, D. H. Electron-induced surface reactions of η^3 -Allyl ruthenium tricarbonyl bromide [$(\eta^3\text{-C}_3\text{H}_5)\text{Ru}(\text{CO})_3\text{Br}$]: contrasting the Behavior of Different Ligands. *J. Phys. Chem. C* **2015**, *119*, 15349–15359.

(52) Spencer, J. A.; Wu, Y.-C.; McElwee-White, L.; Fairbrother, D. H. Electron induced surface reactions of cis-Pt (CO)₂Cl₂: A route to focused electron beam induced deposition of pure Pt nanostructures. *J. Am. Chem. Soc.* **2016**, *138*, 9172–9182.

(53) Tanuma, S.; Powell, C.; Penn, D. Calculations of electron inelastic mean free paths. *Surf. Interface Anal.* **2005**, *37*, 1–14.

(54) Plummer, E.; Salaneck, W.; Miller, J. S. Photoelectron spectra of transition-metal carbonyl complexes: comparison with the spectra of adsorbed CO. *Phys. Rev. B: Condens. Matter Mater. Phys.* **1978**, *18*, 1673.

(55) Barber, M.; Connor, J.; Guest, M.; Hall, M.; Hillier, I.; Meredith, W. High energy photoelectron spectroscopy of transition metal complexes. Part 1.—Bonding in substituted and unsubstituted first row carbonyls. *Faraday Discuss. Chem. Soc.* **1972**, *54*, 219–226.

(56) Moulder, J. F.; Stickle, W. F.; Sobol, P. E.; Bomben, K. D. *Handbook of X-Ray Photoelectron Spectroscopy*; Physical Electronics: Chanhassen, MN, 1995.

(57) van Dorp, W. F.; Wnuk, J. D.; Gorham, J. M.; Fairbrother, D. H.; Madey, T. E.; Hagen, C. W. Electron induced dissociation of trimethyl, methylcyclopentadienyl. platinum, IV.: Total cross section as a function of incident electron energy. *J. Appl. Phys.* **2009**, *106*, 074903.

(58) Engmann, S.; Stano, M.; Matejčík, S.; Ingolfsson, O. Gas phase low energy electron induced decomposition of the focused electron beam induced deposition (FEBIP) precursor trimethyl (methylcyclopentadienyl) platinum (iv)(MeCpPtMe₃). *Phys. Chem. Chem. Phys.* **2012**, *14*, 14611–14618.

(59) May, O.; Kubala, D.; Allan, M. Dissociative electron attachment to Pt (PF₃)₄—a precursor for Focused Electron Beam Induced Processing (FEBIP). *Phys. Chem. Chem. Phys.* **2012**, *14*, 2979–2982.

(60) Wnorowski, K.; Stano, M.; Matias, C.; Denifl, S.; Barszczewska, W.; Matejčík, S. Low-energy electron interactions with tungsten hexacarbonyl–W (CO)₆. *Rapid Commun. Mass Spectrom.* **2012**, *26*, 2093–2098.

(61) Engmann, S.; Stano, M.; Papp, P.; Brunger, M. J.; Matejčík, S.; Ingolfsson, O. Absolute cross sections for dissociative electron attachment and dissociative ionization of cobalt tricarbonyl nitrosyl in the energy range from 0 to 140 eV. *J. Chem. Phys.* **2013**, *138*, 044305.

(62) Marbach, H. Electron beam induced surface activation: a method for the lithographic fabrication of nanostructures via catalytic processes. *Appl. Phys. A: Mater. Sci. Process.* **2014**, *117*, 987–995.

(63) Randolph, S. J.; Fowlkes, J. D.; Rack, P. D. Focused, nanoscale electron-beam-induced deposition and etching. *Crit. Rev. Solid State Mater. Sci.* **2006**, *31*, 55–89.

(64) Knights, A. P.; Coleman, P. G. Secondary electron emission from Ag(100) stimulated by positron and electron impact. *Appl. Surf. Sci.* **1995**, *85*, 43–48.

(65) Ohya, K.; Harada, A.; Kawata, J.; Nishimura, K. Monte Carlo simulation of yield and energy distribution of secondary electrons emitted from metal surfaces. *Jpn. J. Appl. Phys.* **1996**, *35*, 6226–6232.

(66) Gazzadi, G. C.; Mulders, H.; Trompenaars, P.; Ghirri, A.; Affronte, M.; Grillo, V.; Frabboni, S. Focused electron beam deposition of nanowires from cobalt tricarbonyl nitrosyl (Co(CO)₃NO) precursor. *J. Phys. Chem. C* **2011**, *115*, 19606–19611.

(67) Gazzadi, G.; Mulders, J.; Trompenaars, P.; Ghirri, A.; Rota, A.; Affronte, M.; Frabboni, S. Characterization of a new cobalt precursor for focused beam deposition of magnetic nanostructures. *Microelectron. Eng.* **2011**, *88*, 1955–1958.

(68) Koops, H. W. P.; Weiel, R.; Kern, D. P.; Baum, T. High-resolution electron-beam induced deposition. *J. Vac. Sci. Technol., B: Microelectron. Process. Phenom.* **1988**, *6*, 477–481.

(69) Porrati, F.; Sachser, R.; Huth, M. The transient electrical conductivity of W-based electron-beam-induced deposits during growth, irradiation and exposure to air. *Nanotechnology* **2009**, *20*, 195301.

(70) Mulders, J.; Belova, L.; Riazanova, A. Electron beam induced deposition at elevated temperatures: compositional changes and purity improvement. *Nanotechnology* **2011**, *22*, 055302.

(71) Ervin, M.; Nichols, B. Electron beam induced deposition of cobalt for use as single-and multiwalled carbon nanotube growth catalyst. *J. Vac. Sci. Technol. B* **2009**, *27*, 2982–2985.

(72) Fernandez-Pacheco, A.; Serrano-Ramon, L.; Michalik, J. M.; Ibarra, M. R.; De Teresa, J. M.; O'Brien, L.; Petit, D.; Lee, J.; Cowburn, R. P. Three dimensional magnetic nanowires grown by focused electron-beam induced deposition. *Sci. Rep.* **2013**, *3*, 1492.

(73) Cordoba, R.; Sese, J.; De Teresa, J.; Ibarra, M. High-purity cobalt nanostructures grown by focused-electron-beam-induced deposition at low current. *Microelectron. Eng.* **2010**, *87*, 1550–1553.